

Efficient Photodoping of Graphene in Perovskite–Graphene Heterostructure

Sanghoon Kim, Sergey G. Menabde, and Min Seok Jang*

Graphene has been shown to be a prospective platform for active photonic devices with exotic optical properties. Employed in these devices, the graphene photodoping mechanism would allow for the remote spatiotemporal doping control by means of illumination, not restricted by the physical gate electrodes. This paper reports on the efficient graphene photodoping in graphene-CH₃NH₃PbI₃ perovskite heterostructure recently spotlighted for photodetector applications. To maximize the photoresponse, the heterostructure is optimized by systematically introducing additional layers of the self-assembled monolayer of octadecyltrichlorosilane molecules, MoO₃, and poly(3,4-ethylenedioxythiophene) polystyrene sulfonate for improving interfacial charge transfer properties. The photodoping amount estimated from the photocurrent measurements is $2.7 \times 10^{12} \text{ cm}^{-2}$ at zero gate bias—more than twice higher than previously observed in graphene-perovskite heterostructures. Without external gate bias, the estimated graphene Fermi energy varies from 0.37 to 0.43 eV due to photodoping, which is sufficient to operate graphene-based active photonic devices at mid-infrared frequencies, and similar to that typically achievable with the conventional electrostatic gating. Furthermore, this work highlights the missing yet important aspect of the characterization method for the phototransistors with a 2D channel, resulting from the mismatch between the units of the current and power densities.

1. Introduction

Among the numerous ongoing studies on graphene applications, one of the most recently proposed is the employment of graphene as a channel material in the hybrid graphene–perovskite phototransistors.^[1–10] The ultrahigh carrier mobility and unique gapless band structure of graphene perfectly complement the photoactive properties of organohalide perovskite materials, typically having a large absorption cross section,^[11] direct bandgap,^[12] and long charge diffusion length.^[13,14] Besides, when considered separately, both materials have issues when applied for photodetection. For example, graphene-based photodetectors usually suffer from low responsivity, which stems from the fundamentally

limited absorption efficiency of $\approx 2.3\%$ in pristine graphene^[15] and ultrafast carrier recombination,^[16] while the perovskite materials exhibit low photoelectron collection efficiency due to high intrinsic resistivity.^[17] Therefore, combining the advantages of both materials, the graphene–perovskite heterostructures demonstrate superior responsivity^[1–10] and gain.^[7–9]

However, the powerful mix of graphene and organohalide perovskites is promising for active device applications beyond the photodetection and photovoltaics. We point out that the photoinduced variation of carrier concentration, conventionally utilized in the graphene–perovskite phototransistors, can be employed for graphene photodoping, providing a significant variation in its Fermi level in the range from 0.2 to 0.4 eV that would be sufficient to induce a significant change in electronic and optical properties^[18] of graphene. Most notably, the properties of graphene plasmons, which have been actively investigated as an ideal platform for strong light-matter interaction over mid-infrared to THz frequencies,^[19,20] can also be dramatically tuned by photoinduced carrier

variation of graphene.^[21] The photodoping has one particularly important advantage over the conventional electrostatic and chemical doping: it is spatially and temporally reconfigurable by simply changing the illumination pattern and intensity, which opens the possibility of creating a new class of adaptive, nonlinear, and reconfigurable graphene-based photonic devices not restricted by the shape of the physical gate electrodes.

From the perspective of graphene photodoping, we approach the design of the graphene–perovskite heterostructure at a new angle, focusing on high and photosensitive carrier concentration in graphene, instead of typically targeted phototransistor responsivity. In this report, we demonstrate the heterostructure with significantly stronger photoresponse in terms of photoinduced graphene doping as compared to earlier works.

Meanwhile, improving the responsivity of graphene–perovskite photodetectors has been a subject of several recent studies, where different perovskite materials are employed as an active layer, providing efficient light absorption and transport of photogenerated carriers to the graphene channel. However, previous studies have reported on the devices with nonuniformly deposited perovskite, being in the form of islands,^[7] mesh of nanowires,^[8] or thin film of significantly

S. Kim, Dr. S. G. Menabde, Prof. M. S. Jang
School of Electric Engineering
Korea Advanced Institute of Science and Technology
Daejeon 34141, Korea
E-mail: jang.minseok@kaist.ac.kr

 The ORCID identification number(s) for the author(s) of this article can be found under <https://doi.org/10.1002/aelm.201800940>.

DOI: 10.1002/aelm.201800940

varying thickness^[6] of 100–480 nm. This is because of the low surface polar energy of graphene, making it hydrophobic^[22] and not allowing the uniform perovskite film deposition vital for uniform photodoping pattern. Another doping-related problem is the efficiency of electron trapping in the perovskite necessary to reduce the charge recombination. An additional poly(3-hexylthiophene) (P3HT) hole transport layer has been used to resolve this issue in the perovskite solar cells.^[9] However, the employed combination of materials has caused the n-type doping of graphene, shifting the device operation close to the charge neutrality point. Although this might be beneficial for a phototransistor, the requirement of high doping (Fermi level up to 0.4–0.5 eV) necessary for the plasmonic-driven operation is not satisfied. Besides, a structure with gold nanoparticles under the graphene layer has been investigated in order to increase the responsivity.^[10] However, when brought into contact with graphene, gold nanoparticles deteriorate the carrier mobility of the latter^[23] and generally lead to a strong light scattering, both unacceptable for the graphene-based plasmonic devices.

In this study, we demonstrate an optimized heterostructure containing the uniform layers of molybdenum trioxide (MoO₃), poly(3,4-ethylenedioxythiophene) polystyrene sulfonate (PEDOT:PSS), and widely used perovskite material methylammonium lead iodide (CH₃NH₃PbI₃, or MAPbI₃), all deposited on top of the graphene, supported by a self-assembled monolayer (SAM) of octadecyltrichlorosilane (ODTS) molecules. Such heterostructure allows for eliminating the hydrophobicity of graphene, improving the band energy alignment, and increasing the electron trapping in the perovskite, all resulting in the efficient graphene photodoping. We quantify the *p*-type photodoping value Δp in graphene (i.e., the change of carrier concentration under illumination) in the field effect transistor (FET) device as well as rigorously compare the results with the reported earlier for similar devices. Our heterostructure demonstrates both high photodoping of graphene and high sensitivity of doping to the change of the incident power. Estimated photodoping amount is as high as $\Delta p \approx 2.7 \times 10^{12}$ carriers per cm², or 31% increase compared to the unilluminated (dark) state, measured at zero gate bias under the incident power density $F = 7.4 \text{ mW cm}^{-2}$ at 633 nm wavelength; corresponding range of the Fermi level is from 0.37 to 0.43 eV. Demonstrated carrier concentration levels are approximately three times higher than that observed in previous studies under similar experimental conditions,^[7–9] while the responsivity of our device is also high, reaching $2 \times 10^4 \text{ A W}^{-1}$. Furthermore, under a nonzero gate bias of $V_g = 60 \text{ V}$, the photodoping reaches 110% of the dark-state carrier concentration ($\Delta p \approx 5.3 \times 10^{12} \text{ cm}^{-2}$), corresponding to the Fermi level range from 0.26 to 0.39 eV (50% increase by photodoping). Demonstrated variation of the doping in graphene, provided solely by illumination without the electrostatic gating, proves the feasibility of graphene–perovskite photodoping technique and provides the pathway toward a new class of active reconfigurable plasmonic devices.

2. Results and Discussion

The structure of our FET device is shown in **Figure 1a**, and its energy band diagram is presented in **Figure 1b** along with the

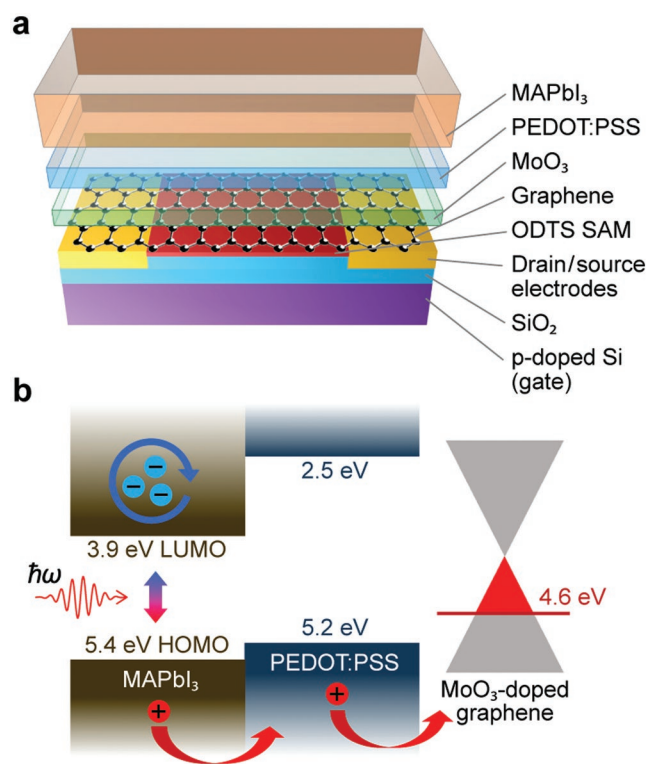


Figure 1. a) The schematic of the FET device with graphene channel. b) Band diagram of the heterostructure for the efficient *p*-type photodoping of graphene.

carrier transport schematics. Perovskite material functions as an active layer where the photoexcited electron–hole pairs are generated, and the *p*-type photodoping of graphene is then induced by the holes transported from the perovskite (**Figure 1b**). Efficient hole transport and injection into the graphene is provided by several intermediate layers with properly aligned energy bands, while the electrons stay trapped in the perovskite. We have optimized the heterostructure by altering the fabrication techniques and materials in order to enhance its photodoping performance.

Similar to numerous studies demonstrated the improved carrier mobility in graphene, we use the ODTS SAM to isolate^[24] graphene from the insulating SiO₂ layer formed on the heavily *p*-doped Si substrate. SAM is widely used to block the orbital interaction between the SiO₂ and graphene,^[6,25,26] increasing its carrier mobility, as demonstrated in **Figure 2a** by the photoenhanced drain current (I_d) in the devices with and without SAM (measured at a gate voltage $V_g = 0 \text{ V}$ and source-drain bias $V_{sd} = 1 \text{ V}$). The Raman spectrum of the chemical vapor deposition (CVD) graphene on SAM is shown in **Figure 2b**, demonstrating a good quality of the material with a low number of impurities.

The issue related to the low wettability of graphene (**Figure 2c**, left) is solved by depositing a 2 nm thick layer of MoO₃ on the graphene (**Figure 2c**, right), as suggested in the recent work on graphene–perovskite solar cells.^[27] We verify the effect of the MoO₃ layer of different thickness by contact angle measurements as shown in the top row of **Figure 2c**, confirming that the 2 nm thick layer is enough to uniformly cover the graphene and significantly improve its wettability. We note that a thicker layer

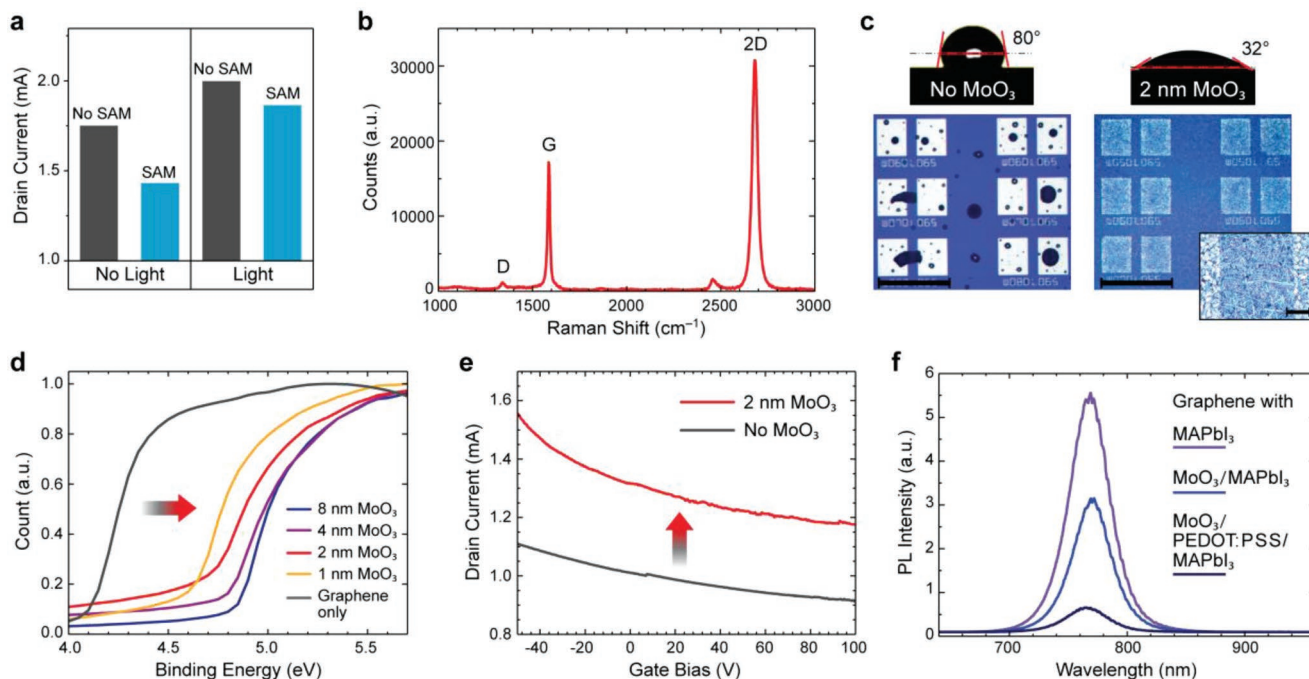


Figure 2. a) Photoinduced I_d enhancement in the graphene–perovskite-only device with and without ODTs SAM; $V_{sd} = 1$ V, $V_g = 0$ V, $F = 0.5$ mW cm⁻². b) Raman spectrum of CVD graphene after its wet transfer on the substrate with SAM. c) Effect of the MoO₃ layer on graphene wettability: (top) snapshots of a water droplet on graphene with and without a MoO₃ layer, and (bottom) corresponding optical images of spin-coated perovskite on graphene. The scale bar is 500 μ m; inset: graphene channel of the FET device with uniformly deposited perovskite (the scale bar is 10 μ m). d) UPS measurements of the electron work function in the graphene doped by a MoO₃ layer of different thickness (colored), and that of bare graphene (gray). e) FET transfer characteristics without MoO₃ (gray), and with 2 nm layer of MoO₃ (red) under no illumination; $V_{sd} = 1$ V. f) PL intensity of the heterostructures with different additional layers between the graphene and perovskite.

of MoO₃ may hinder hole extraction from the perovskite, as suggested in the previous study.^[27] The layer of MoO₃ also plays an important role for the energy bands alignment in the heterostructure (Figure 1b). As shown in Figure 2d, the ultraviolet photoelectron spectroscopy (UPS) measurements show that the work function of graphene can be shifted by nearly 0.6–0.8 eV due to the thin layer of MoO₃ deposited on graphene. This surface transfer doping method, unlike other surface treatment methods such as ultraviolet/ozone (UVO) treatment^[27] and vacuum annealing,^[28] permanently changes the surface energy of the graphene using the interaction between the dopant layer and the π -orbitals of carbon atoms in graphene. Proper band alignment significantly increases the carrier transport efficiency, as shown in Figure 2e, which compares the transfer characteristics for the devices with and without the MoO₃ layer.

Another step toward the enhanced hole transport efficiency is the deposition of the PEDOT:PSS layer on the MoO₃-doped graphene, which plays a role of the electron blocking layer,^[27,29] while further improving the band alignment between the perovskite and graphene (Figure 1b). The photoluminescence (PL) intensity in Figure 2f demonstrates the significant suppression of carrier recombination with additional layers introduced between the graphene and perovskite. For example, the graphene/MoO₃/MAPbI₃ heterostructure has a 44% lower PL intensity compared with that without MoO₃. The additional 30 nm thick layer of PEDOT:PSS further reduces the PL intensity by 81%, resulting in total 89% reduction of the PL intensity compared to the graphene/MAPbI₃ only. This drastic

reduction of the PL intensity, along with the energy bands alignment (Figures 1b and 2d,e) and enhanced photoresponse of the FET device (Figure 3), demonstrate that the p-type photo-doping of graphene is indeed due to the efficient photo-holes transport, and not electrostatic effects.

Here, we add the deionized (DI) water into the as-purchased 1.5 wt% PEDOT:PSS dispersion with the volume ratio 1:1 to achieve a thinner film formation by spin coating as suggested in a previous works on perovskite solar cells.^[29] Figure 3 demonstrates the PEDOT:PSS effect on the photocurrent in the graphene–perovskite FET devices when introduced into the graphene/MoO₃/MAPbI₃ heterostructure. The deposition of PEDOT:PSS from as-purchased dispersion results in the formation of a 50 nm thick layer, and provides the slightly increased photo/dark current ratio of 18% at $V_g = 0$ (Figure 3b), compared to just 7% in the device without PEDOT:PSS (Figure 3a). At the same time, the deposition of a 30 nm thick layer of PEDOT:PSS (from 0.75 wt% dispersion) increases the photo/dark current ratio up to 39% under the same experimental conditions (Figure 3c). These results are in a perfect agreement with the recent study^[29] demonstrating that PEDOT:PSS, when deposited from the water-diluted dispersion of lower concentration, has better interface contact with MAPbI₃ and lower energy level of highest occupied molecular orbital (HOMO), providing a better match to the HOMO energy level of MAPbI₃. Both effects result in more efficient hole transport,^[29] which is reflected in significantly better photocurrent generation performance evident from Figure 3b,c.

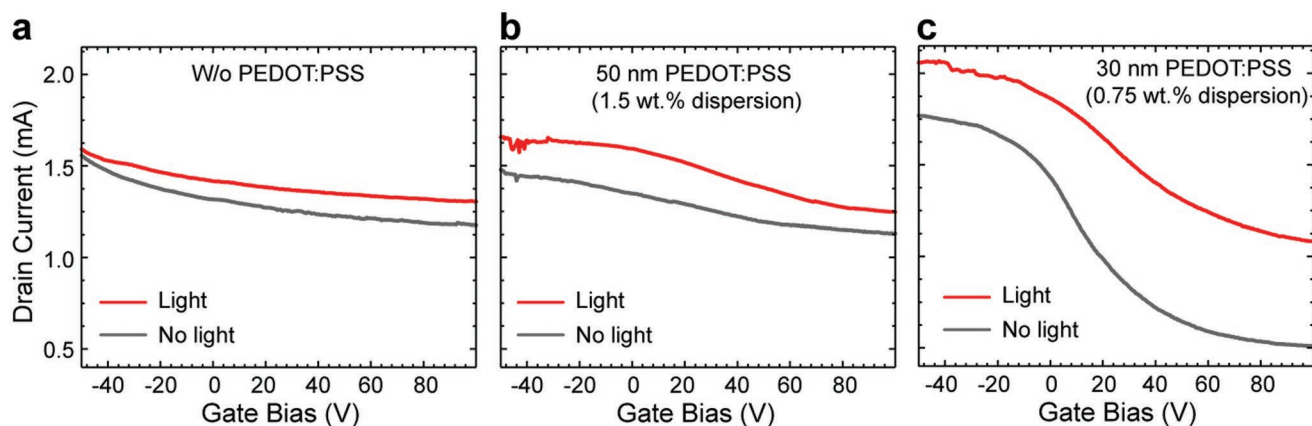


Figure 3. Transfer characteristics of our FET device at $V_{sd} = 1$ V, without and under $F = 0.5$ mW cm^{-2} illumination: a) graphene/ MoO_3 / MAPbI_3 heterostructure without PEDOT:PSS; b) heterostructure with 50 nm thick PEDOT:PSS layer formed from as-purchased dispersion (1.5 wt%); c) same structure with 30 nm thick PEDOT:PSS layer formed from the 1:1 water-diluted dispersion (0.75 wt%).

Figure 4a,b shows the SEM images of the complete heterostructure with ≈ 400 nm thick top layer of MAPbI_3 having a nanorod morphology. The MAPbI_3 on PEDOT:PSS is formed with sequential deposition method,^[30] which has been employed to form the perovskite nanowires^[31,32]: the layer of PbI_2 is first spin-coated from its solution in dimethylformamide (DMF), followed by the second spin coating of an isopropanol solution of $\text{CH}_3\text{NH}_3\text{I}$. It has been demonstrated^[31,32] that the nanowire/nanorod morphology is caused by the presence of the small amount of polar aprotic solvent (in this case, the DMF) defining the perovskite growth direction. The crystalline structure and deposition uniformity of MAPbI_3 is then verified with both electron (Figure 4a,b) and optical (Figure 2c, right) micrograph, and its X-ray diffraction (XRD) spectra shown in Figure 4c. MAPbI_3 is known to form other morphologies like nanocubes^[31,33] or nanoplates^[33] which have been reported to have similar light absorbing efficiency compared to the nanorod morphology.^[31,32] The XRD data of our sample demonstrates the strong peaks at 14.0° , 19.8° , 23.42° , 28.34° , 31.69° in good agreement with the tetragonal perovskite phase^[32–34] with (110), (112), (211), (220), (222) lattice planes, respectively. Other peaks have been associated with the intermediate phase, indicating the incomplete process of the perovskite formation.^[34] Besides,

there exists the diffraction peak at 12.6° corresponding to the (001) lattice plane of PbI_2 , signaling either the incomplete conversion^[33] or the decomposition of the intermediate phase^[34] formed during the MAPbI_3 preparation (see Experimental Section).

In order to evaluate the doping levels in graphene, we performed the photocurrent measurements of our FET device under the different illumination and gate bias. Figure 5a shows the measured transfer characteristics at dark and illuminated states under $F = 0.5$ and 7.4 mW cm^{-2} . Figure 5b shows the photo/dark current ratio, approximately equal to the relative amount of photodoping (as explained in further detail below), directly obtained from the transfer characteristics. Our device demonstrates 31% increase of carrier concentration at zero V_g , and as much as 110% at $V_g > 60$ V, meaning the twofold increase of carrier concentration in graphene under relatively low 7.4 mW cm^{-2} illumination. The photoresponse time of our device is similar to that of other graphene–perovskite phototransistors (See Supporting Information).

We obtain the photoinduced variation in graphene carrier density Δp from the FET transfer characteristics using the two independent methods: 1) using the charge–capacitance relation for the accumulated charge in graphene (at constant drain

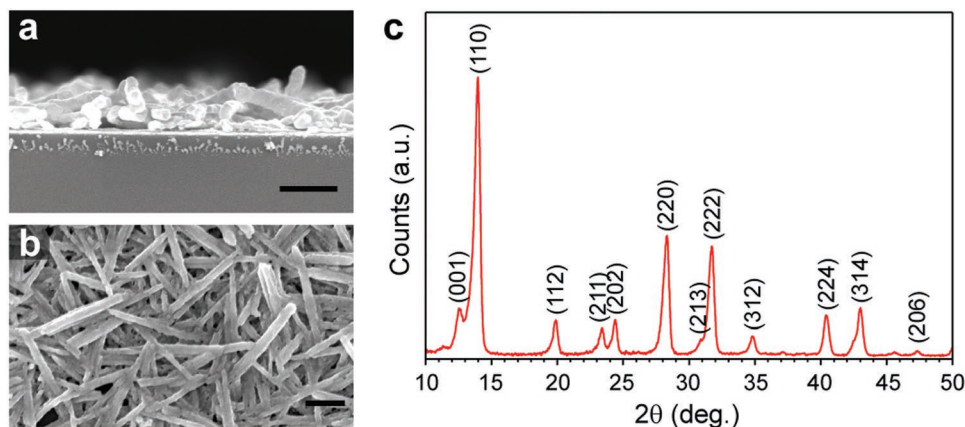


Figure 4. SEM images of the heterostructure (the FET channel): a) cross section, b) top view, showing the ≈ 400 nm thick layer of perovskite having the nanorod morphology; the scale bar is 1 μm . c) XRD spectra of the perovskite.

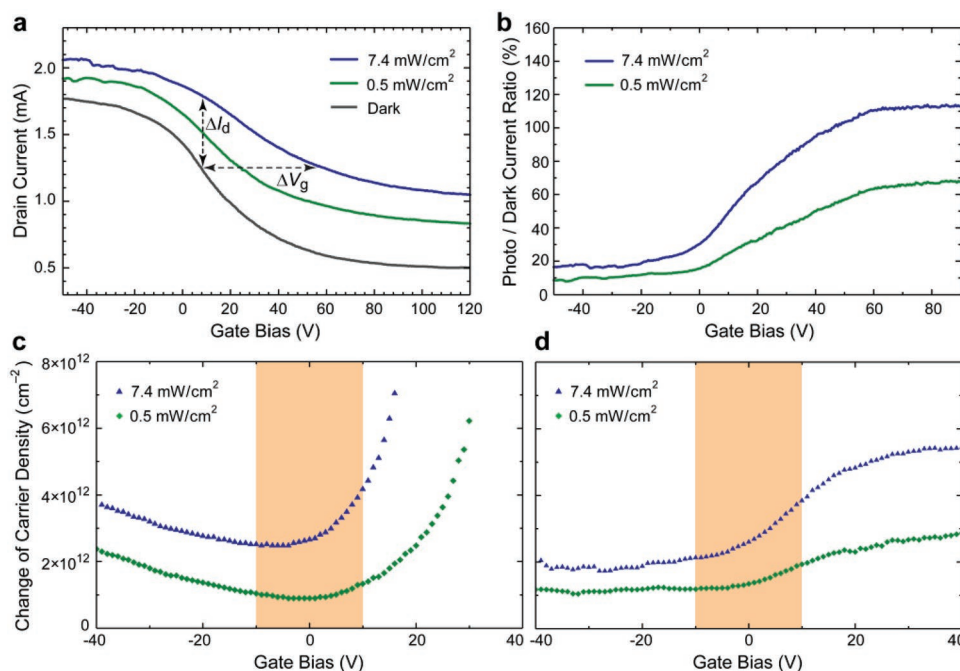


Figure 5. a) Transfer characteristics of our FET device at different illumination power density F ; arrows show the two methods of photodoping calculation: from the charge–capacitance relation (ΔV_g at constant I_d), and from the Ohm's law ($\Delta I_d = I_{ph}$ at constant V_g). b) Photo/dark current ratio as a function of V_g under different illumination. c) Photodoping amount Δp in graphene calculated from the charge–capacitance relation. d) Same as in (c), calculated from the Ohm's law.

current, illustrated as the horizontal arrow in Figure 5a), and 2) applying the Ohm's law for the drain current (at constant gate voltage, the vertical arrow in Figure 5a). In both methods, it is not necessary to know the value of the carrier mobility in graphene, which we assume constant in each case. The photovoltaic effect in our device can be neglected due to the symmetrical material of electrodes and spatial illumination profile.

First, the photodoping value Δp is obtained from the charge–capacitance relation for the total accumulated charge in graphene $Q \equiv epA = CV_g$, where A is the surface area of the graphene channel, C is the capacitance. The parallel plate capacitance is given by $C = \epsilon A/d$, where ϵ and d are the dielectric permittivity and thickness of the insulating SiO_2 layer, respectively. Then, the relation between the change in gate voltage and the charge density variation (at constant current and carrier mobility) is obtained as $\Delta p = \epsilon \Delta V_g / ed$. The carrier concentration in graphene without illumination at given V_g is then $p_0 = \epsilon(V_{\text{Dirac}} - V_g) / ed$, where V_{Dirac} is the Dirac gate voltage corresponding to the charge neutrality point.

Second, according to the Ohm's law, the dark current is given by $I_{\text{dark}} = ep_0 \mu V_{sd} W/L$, where e is the elementary charge, μ is the carrier mobility in graphene, and W and L are the width and length of the graphene FET channel, respectively. Assuming constant carrier mobility, the photocurrent is approximated as $I_{ph} = e \Delta p \mu V_{sd} W/L$, and the photo/dark current ratio, reflecting the relative amount of photodoping, is approximated as

$$\frac{I_{ph}}{I_{dark}} \approx \frac{\Delta p}{p_0}.$$

Therefore, the variation of carrier density in graphene is given by

$$\Delta p = \frac{I_{ph}}{I_{dark}} \frac{\epsilon}{ed} (V_{\text{Dirac}} - V_g).$$

We note that both described methods have limitations, such as the carrier mobility assumed independent on the Fermi level and that the Dirac voltage must be known to obtain the initial carrier concentration. In particular, it is quite typical that the Dirac voltage cannot be measured precisely in the graphene–perovskite FET devices, therefore in such cases, we use the maximum reported V_g value instead (50 V, ref. [8]). Thus, for our device, we assume $V_{\text{Dirac}} = 120$ V.

The photoinduced Δp , calculated with the two different methods, is shown in Figure 5c,d for the charge–capacitance and Ohm's law approaches, respectively. We note that both methods agree well at small gate voltages $|V_g| < 10$ V (highlighted by the shaded areas); therefore, we conclude that the evaluation of the photodoping at $V_g = 0$ V is the most correct. At zero gate bias, our device has estimated $p_0 \approx 8.6 \times 10^{12} \text{ cm}^{-2}$ and demonstrates $\Delta p \approx 2.7 \times 10^{12} \text{ cm}^{-2}$ under 7.4 mW cm^{-2} illumination, which corresponds to the operational range of the Fermi level from 0.37 to 0.43 eV. The highest relative amount of photodoping of 110% is observed at $V_g = 60$ V, closer to the Dirac point, where the lower $p_0 \approx 4.3 \times 10^{12} \text{ cm}^{-2}$ limits the maximum carrier concentration to $9.1 \times 10^{12} \text{ cm}^{-2}$, although providing a larger variation of the Fermi level from 0.26 to 0.39 eV. Here, we note that proper design of the initial carrier concentration in graphene is of key importance for the operational photodoping levels, particularly in the devices with no electrostatic gate.

To benchmark the photodoping performance of our device, we analyze the published data for the devices based on the multilayer

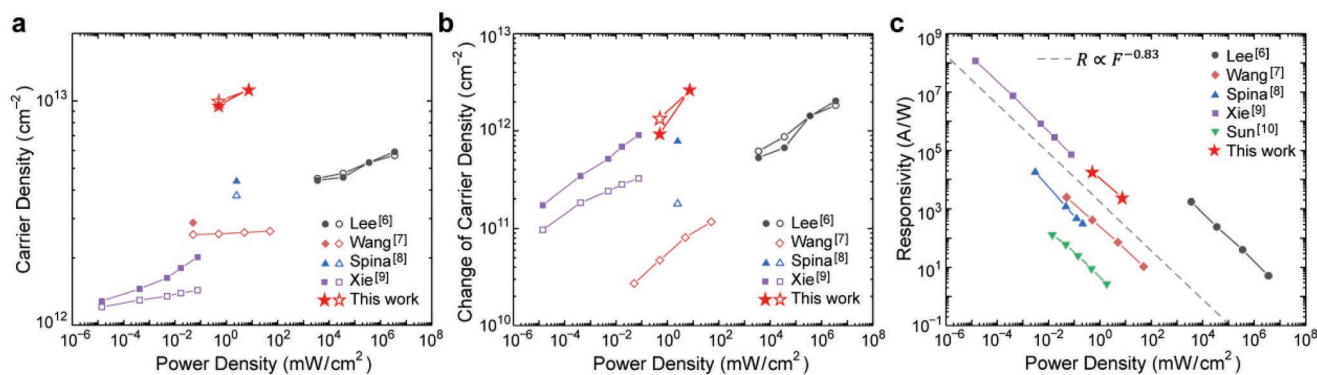


Figure 6. a) Carrier density in the graphene channel of the FET as a function of the incident power density for our and reported devices, obtained by the two methods: charge–capacitance relation (filled symbols) and Ohm’s law (open symbols); all data is for zero gate bias. b) Photodoping of graphene relative to the dark state, for the same sets of data as in (a). c) Normalized (to our device) responsivity of the FET devices according to the channel length and applied source-drain bias in each case; note the common power-law $R \propto F^{-0.83}$ followed by all devices.

graphene–perovskite heterostructures.^[6–9] We obtain the photodoping Δp and the total carrier concentration $p = p_0 + \Delta p$ at zero gate bias for the reported devices by analyzing the published data of the photocurrent measurements (for details, see Supporting Information). We summarize the results for calculated p and Δp in **Figure 6a,b**, respectively. Each figure contains two sets of data, obtained with the charge–capacitance relation (filled symbols) and Ohm’s law (open symbols). Our device simultaneously demonstrates the superior levels of doping and photodoping (star symbols in Figure 6a,b), which are both necessary for photonic applications. Estimated amount of photodoping Δp is more than two times higher than demonstrated in other devices under similar (or even higher) incident power density. The sensitivity of the photodoping to the incident power $\Delta p/F$ at our experimental conditions is estimated as $\approx 2.3 \times 10^{12}$ and $\approx 3.5 \times 10^{11}$ free carriers per mW under 0.5 and 7.4 mW cm^{-2} illumination, respectively.

We would like to note that, for the graphene-based FETs, the carrier concentration in graphene as a function of the incident power density demonstrates the efficiency of carrier generation and transport in a more accurate way than the commonly used responsivity $R = I_{\text{ph}}/(FA)$. This is particularly important since the photocurrent (hence, the responsivity) is a function of the source-drain bias and geometry of the FET, all vastly varying from case to case, and not contributing to the efficiency of carrier generation and transport. Furthermore, the by-definition equal surface area normalization for the current (volume current density) and power (incident power density), does not hold for the FET devices with a 2D channel. The responsivity of such devices contains the normalization factor V_{sd}/L^2 that allows for the proper comparison between the devices of different geometry under different measurement conditions (see Supporting Information).

We calculate the responsivity for all analyzed devices, normalizing it to the parameters of our device ($V_{\text{sd}} = 1 \text{ V}$, $L = 50 \text{ }\mu\text{m}$), as summarized in Figure 6c. Interestingly, all analyzed graphene–perovskite devices exhibit the similar power-law dependence $R \propto F^{-0.83}$ (dotted line in Figure 6c). To the best of our knowledge, that general dependency has not been reported so far and requires further investigation. We speculate that this is a consequence of similar internal quantum efficiency of employed perovskite materials as well as all devices operating

at the photocurrent saturation regime. The current saturation in the graphene–perovskite photodetectors has not been clearly attributed to certain phenomena, though it has been suggested that it is mainly due to the screening effect^[35,36] and nonlinear light absorption due to the enhanced carrier recombination.^[37]

3. Conclusion

The carrier concentration in graphene defines its optoelectronic properties. By realizing the efficient photodoping scheme, one can actively control graphene properties by means of illumination with no need for the electrostatic gating. We demonstrate the graphene–perovskite heterostructure optimized for the efficient photodoping of graphene: graphene/MoO₃/PEDOT:PSS/MAPbI₃ on the Si/SiO₂ substrate with ODTs SAM. We quantitatively analyze the carrier concentration and Fermi level in graphene under illumination, using two independent calculation methods. By rigorous comparison with previous studies, we show that our device has approximately twofold increased photodoping amount at zero gate bias. The estimated graphene Fermi level changes from 0.37 to 0.43 eV under moderate 7.4 mW cm^{-2} illumination, which is sufficient to operate graphene-based active photonic devices. In the absence of the gate electrodes, the photodoping potentially allows for the reconfigurable doping patterns of unrestricted dimensions and shape across the large areas of graphene. This promising functionality is important for the development of the gateless graphene-based active photonic devices.

4. Experimental Section

Device Fabrication: First, a 300 nm thick SiO₂ layer was formed on the heavily p-doped silicon substrate by wet-oxidation. The substrate was patterned with the photolithography and then etched using the buffered oxide etchant (1:6, J. T. Baker). Then, a 100 nm thick aluminum layer was deposited on the substrate with the thermal evaporator (KVE-T2010, Korea Vacuum Tech.) to make the bottom electrode. Next, source and drain electrodes were made by depositing 15 nm/75 nm chrome/gold on the substrate with photolithography and subsequent thermal evaporation. Next, a SAM of octadecyltrichlorosilane (ODTS, Sigma-Aldrich) was spin-coated upon the substrate to separate the SiO₂ and graphene. Afterward, a single layer of CVD-grown graphene on a

copper foil (Graphene Square) was transferred to the substrate with conventional PMMA-assisted wet transfer technique. The substrate was then patterned by the photolithography, and graphene was etched with inductively coupled plasma asher (KVIA-3008DC, Korea Vacuum Tech.) to form the FET channel. This substrate was annealed in a vacuum furnace (Sungrim Industrial) under 200 °C for 2 h. The MoO₃ layer was deposited with the thermal evaporator (Korea Vacuum Tech.), using the quartz crystal microbalance measurements to control its thickness with a fraction of an angstrom precision; and it was annealed on the hotplate under 150 °C for 10 min. Then, the 1:1 D.I. water-diluted PEDOT:PSS dispersion (Clevios P VP Al 4083, 1.5 wt%) was spin-coated on the prepared substrate at 5000 rpm for 30 s, forming a 30 nm layer.

Perovskite Synthesis: MAPbI₃ layer was formed on the prepared substrate with the two-step spin coating method in the glove box. To prepare the MAPbI₃, 461 mg of PbI₂ (Sigma-Aldrich) was dissolved in 1 mL of the DMF (Sigma-Aldrich) (for the first spin coating), and 15.9 mg of CH₃NH₃I was dissolved in 1 mL of the IPA (for the second spin coating). The first spin coating was performed at 4000 rpm for 30 s, and the second one at 3000 rpm for 30 s, forming 400 nm thick layer of MAPbI₃.

Photocurrent Measurements: As a tunable illumination source, a fiber-coupled 10 mW diode laser at 635 nm, electronic variable optical attenuator (ThorLabs V600F), collimator to outcouple the light, and 10X objective lens to form the spot of 100 μm diameter at the 50 × 50 μm² FET channel was used.

Supporting Information

Supporting Information is available from the Wiley Online Library or from the author.

Acknowledgements

S.K. and S.G.M. contributed equally to this work. This work was supported by the Samsung Research Funding Center of Samsung Electronics under Project Number SRFC-IT1702-14. S.G.M. acknowledges support from the Global Center for Open Research with Enterprise (GCORE, Grant number: N11180017) funded by the Ministry of Science and ICT.

Conflict of Interest

The authors declare no conflict of interest.

Keywords

graphene, graphene photonics, heterostructures, perovskite, photodoping

Received: December 17, 2018

Published online:

- [1] F. Xia, T. Mueller, Y. Lin, A. Valdes-Garcia, P. Avouris, *Nat. Nanotechnol.* **2009**, *4*, 839.
[2] G. Konstantatos, M. Badioli, L. Gaudreau, J. Osmond, M. Bernechea, F. P. Garcia de Arquer, F. Gatti, F. H. L. Koppens, *Nat. Nanotechnol.* **2012**, *7*, 363.

- [3] W. Guo, S. Xu, Z. Wu, N. Wang, M. M. T. Loy, S. Du, *Small* **2013**, *9*, 3031.
[4] H. Xu, L. Wu, Q. Feng, N. Mao, C. Wang, J. Zhang, *Small* **2014**, *10*, 2300.
[5] D.-H. Kwak, D.-H. Lim, H.-S. Ra, P. Ramasamy, J.-S. Lee, *RSC Adv.* **2016**, *6*, 65252.
[6] Y. Lee, J. Kwon, E. Hwang, C.-H. Ra, W. J. Yoo, J.-H. Ahn, J. H. Park, J. H. Cho, *Adv. Mater.* **2015**, *27*, 41.
[7] Y. Wang, Y. Zhang, Y. Lu, W. Xu, H. Mu, C. Chen, H. Qiao, J. Song, S. Li, B. Sun, Y. Cheng, Q. Bao, *Adv. Opt. Mater.* **2015**, *3*, 1389.
[8] M. Spina, M. Lehmann, B. Náfrádi, L. Bernard, E. Bonvin, R. Gaál, A. Magrez, J. Forró, E. Horváth, *Small* **2015**, *11*, 4824.
[9] C. Xie, F. Yan, *ACS Appl. Mater. Interfaces* **2017**, *9*, 1569.
[10] Z. Sun, L. Aigouybcd, Z. Chen, *Nanoscale* **2016**, *8*, 7377.
[11] M. M. Lee, J. Teuscher, T. Miyasaka, T. N. Murakami, H. J. Snaith, *Science* **2012**, *338*, 643.
[12] J.-Y. Jeng, Y.-F. Chiang, M.-H. Lee, S.-R. Peng, T.-F. Guo, P. Chen, T.-C. Wen, *Adv. Mater.* **2013**, *25*, 3727.
[13] S. D. Stranks, G. E. Eperon, G. Grancini, C. Menelaou, M. J. P. Alcocer, T. Leijtens, L. M. Herz, A. Petrozza, H. J. Snaith, *Science* **2013**, *342*, 341.
[14] G. Xing, N. Mathews, S. Sun, S. S. Lim, Y. M. Lam, M. Grätzel, S. Mhaisalkar, T. C. Sum, *Science* **2013**, *342*, 344.
[15] R. R. Nair, P. Blake, A. N. Grigorenko, K. S. Novoselov, T. J. Booth, T. Stauber, N. M. R. Peres, A. K. Geim, *Science* **2008**, *320*, 1308.
[16] J. C. Johannsen, S. Ulstrup, F. Cilento, A. Crepaldi, M. Zacchigna, C. Cacho, I. C. Turcu, E. Springate, F. Fromm, C. Roidel, T. Seyller, F. Parmigiani, M. Grioni, P. Hofmann, *Phys. Rev. Lett.* **2013**, *111*, 027403.
[17] E. Horváth, M. Spina, Z. Szekrényes, K. Kamarás, R. Gaal, D. Gachet, L. Forró, *Nano Lett.* **2014**, *14*, 6761.
[18] A. H. Castro Neto, F. Guinea, N. M. R. Peres, K. S. Novoselov, A. K. Geim, *Rev. Mod. Phys.* **2009**, *81*, 109.
[19] V. W. Brar, M. S. Jang, M. Sherrott, J. J. Lopez, H. A. Atwater, *Nano Lett.* **2013**, *13*, 2541.
[20] S. Kim, M. S. Jang, V. W. Brar, Y. Tolstova, K. W. Mauser, H. A. Atwater, *Nat. Commun.* **2016**, *7*, 12323.
[21] L. Ju, J. Velasco Jr., E. Huang, S. Kahn, C. Nosiaglia, H.-Z. Tsai, W. Yang, T. Taniguchi, K. Watanabe, Y. Zhang, G. Zhang, M. Crommie, A. Zettl, F. Wang, *Nat. Nanotechnol.* **2014**, *9*, 348.
[22] M. Annamalai, K. Gopinadhan, S. A. Han, S. Saha, H. J. Park, E. B. Cho, B. Kumar, A. Patra, S.-W. Kim, T. Venkatesan, *Nanoscale* **2016**, *8*, 5764.
[23] V. Tjoa, W. Jun, V. Dravid, S. Mhaisalkar, N. Mathews, *J. Mater. Chem.* **2011**, *21*, 15593.
[24] Y. Ito, A. A. Virkar, S. Mannsfeld, J. H. Oh, M. Toney, J. Locklin, Z. Bao, *J. Am. Chem. Soc.* **2009**, *131*, 9396.
[25] M. Lafkoti, B. Krauss, T. Lohmann, U. Zschieschang, H. Klauk, K. Klitzing, J. H. Smet, *Nano Lett.* **2010**, *10*, 1149.
[26] X. Wang, J. Xu, C. Wang, J. Du, W. Xie, *Adv. Mater.* **2011**, *23*, 2464.
[27] H. Sung, N. Ahn, M. S. Jang, J.-K. Lee, H. Yoon, N.-G. Park, M. Choi, *Adv. Energy Mater.* **2016**, *6*, 1501873.
[28] Z. Xu, Z. Ao, D. Chu, A. Younis, C. M. Li, S. Li, *Sci. Rep.* **2015**, *4*, 6450.
[29] a) C. Wang, C. Zhang, S. Tong, J. Shen, C. Wang, Y. Li, S. Xiao, J. He, J. Zhang, Y. Gao, J. Yang, *J. Phys. Chem. C* **2017**, *121*, 6575; b) C. Wang, C. Zhang, S. Tong, H. Xia, L. Wang, H. Xie, Y. Gao, J. Yang, *J. Phys. D: Appl. Phys.* **2018**, *51*, 025110.
[30] J. Burschka, N. Pellet, S.-J. Moon, R. Humphry-Baker, P. Gao, M. K. Nazeeruddin, M. Grätzel, *Nature* **2013**, *499*, 316.
[31] J.-H. Im, J. Luo, M. Franckevičius, N. Pellet, P. Gao, T. Moehl, S. M. Zakeeruddin, M. K. Nazeeruddin, M. Grätzel, N.-G. Park, *Nano Lett.* **2015**, *15*, 2120.

- [32] A. A. Petrov, N. Pellet, J.-Y. Seo, N. A. Belich, D. Y. Kovalev, A. V. Shevelkov, E. A. Goodilin, S. M. Zakeeruddin, A. B. Tarasov, M. Graetzel, *Chem. Mater.* **2017**, *29*, 587.
- [33] Y. Fu, F. Meng, M. B. Rowley, B. J. Thompson, M. J. Shearer, D. Ma, R. J. Hamers, J. C. Wright, S. Jin, *J. Am. Chem. Soc.* **2015**, *137*, 5810.
- [34] X. Guo, C. McCleese, C. Kolodziej, A. C. S. Samia, Y. Zhao, C. Burda, *Dalton Trans.* **2016**, *45*, 3806.
- [35] W. Budde, *Appl. Opt.* **1983**, *22*, 1780.
- [36] T. Mueller, F. Xia, F. Avouris, *Nat. Photonics* **2010**, *4*, 297.
- [37] a) J. Ding, S. Du, X. Cheng, L. Jing, Y. Zhao, Z. Zuo, H. Cui, X. Zhan, *Mater. Chem. Phys.* **2018**, *204*, 222; b) Z. Lian, Q. Yan, Q. Lv, Y. Wang, L. Liu, L. Zhang, S. Pan, Q. Li, L. Wang, J.-L. Sun, *Sci. Rep.* **2015**, *5*, 16563; c) R. H. Bube, C.-T. Ho, *J. Appl. Phys.* **1966**, *37*, 4132; d) K. Domanski, W. Tress, T. Moehl, M. Saliba, M. K. Nazeeruddin, M. Grätzel, *Adv. Funct. Mater.* **2015**, *25*, 6936.